Journal of Power Sources 195 (2010) 2870–2876

Contents lists available at ScienceDirect

Journal of Power Sources

journal homepage: www.elsevier.com/locate/jpowsour

The effects of crystallization parameters on the ionic conductivity of a lithium aluminum germanium phosphate glass–ceramic

Joykumar S. Thokchom*, Binod Kumar

Electrochemical Power Group, Metals and Ceramics Division, University of Dayton Research Institute, Dayton, OH 45469, USA

ARTICLE INFO

Article history:
Received 24 September 2009
Received in revised form 6 November 2009
Accepted 9 November 2009
Available online 14 November 2009

Keywords:
LAGP glass
Crystallization parameters
Glass–ceramic
Microstructure
Superionic conductivity
Space charge and blocking effects

ABSTRACT

This paper reports on a relationship between the conductivity and crystallization parameters (time and temperature) of a lithium aluminum germanium phosphate (LAGP) glass–ceramic. To study the relationship, a specific formulation of the LAGP [$Li_{1+x}Al_xGe_{2-x}(PO_4)_3$ ($x = 0.5$)] glass was chosen. The glass was crystallized at different temperatures and times and it was characterized for microstructures and ionic conductivity. The highest total conductivity of the glass–ceramic material, 4.22×10^{-3} S cm^{-1} at 27 °C, was obtained by crystallizing the glass at 825 °C for 8 h. The superionic conductivity in the specimens is attributed to the space charge-mediated effect resulting from the presence of the dielectric phase ($AlPO_4$). The impurity phase $AlPO_4$ imparted a characteristic non-linearity in the Arrhenius plots. A decrease in conductivity with an increase in crystallization temperature and time was observed. The observed conductivity was explained on the basis of the blocking effect resulting from an increased concentration or size of the impurity phase, $AlPO_4$. The thermally unstable nature of the LAGP is reflected by the relationship between the conductivity and the crystallization parameters. Conductivity of the glass–ceramic is believed to be significantly affected by the space charge and blocking effects that originate from and relate to the crystallization temperature and time.

1. Introduction

A need for high power density portable power sources for items ranging from small devices (electronic gadgets) to large systems (electric vehicles) exists. State-of-the art commercial lithium ion batteries provide the highest energy density of about 160 Wh kg^{-1}. They employ liquids as electrolytes, which limit their performance, scale-up (due to flammability of the electrolytes), and life cycle (primarily linked to thermal instability of lithium salt). In spite of these technical issues, liquid electrolytes remain the choice for these batteries because they possess high lithium ion conductivity and lack a comparable solid lithium ion conductor. The lithium battery community is exploring lithium–air and lithium–water chemistries to further improve the energy density. However, their development and commercialization have been impeded due to two major technical barriers: the lack of conductive and chemically stable membranes to isolate the lithium metal from the atmospheric gases, and efficient air cathodes [1]. These challenges inspire researchers worldwide to develop a stable, solid electrolyte having a conductivity comparable to the liquid electrolytes.

Solid ionic conductors based on a $LiM_2(PO_4)_3$ [M = Ti, Ge, etc. is a metal] structure analogous to a Nasicon-type structure [2–4] are among the most promising groups of oxide-based solid lithium ion conductors investigated in recent years. They possess certain advantages in terms of electrical conductivity, mechanical strength, and stability in ambient atmosphere compared to other solid electrolytes. Superionic glass–ceramic materials [lithium aluminum titanium phosphate (LATP) and lithium aluminum germanium phosphate (LAGP)], which are respective derivatives of $LiTi_2(PO_4)_3$ and $LiGe_2(PO_4)_3$, were originally developed by Fu [5,6] and subsequently by other investigators [7–10]. The published results on these glass–ceramics revealed that they consist of a mixture of highly conductive $Li_{1-x}Al_xTi_{2-x}(PO_4)_3$ ($x = 0.275$) and $Li_{1-x}Al_xGe_{2-x}(PO_4)_3$ ($x = 0.5$) crystalline phases and dielectric phases (Li_2O and $AlPO_4$), aggregated mainly at the grain boundary region. Nasison-type structure consists of two polyhedra-TiO_6 octa- and PO_4 tetra-hedra, linked by their corners to form a $[Ti_2(PO_4)_3]^-$ or $[Ge_2(PO_4)_3]^-$ rigid skeleton that provides a three-dimensional tunnel wherein the Li^+ can reside and migrate through.

The presence of the dielectric phases (Li_2O and $AlPO_4$) in the LATP and LAGP systems have been detected, identified, and reported in the literature [5,7–13]. The roles of Li_2O and $AlPO_4$ in the conduction of lithium ion in terms of space charge and blocking effects are of special interest in these heterogeneous and monoionically conducting systems. Recently, few attempts have been made to investigate the roles of these impurities in the LATP and LAGP systems [11–13]. It was suggested [12] that the adsorption and desorption of the electroactive species (Li^+) onto the dielectric,

* Corresponding author. Tel.: +1 937 229 4355; fax: +1 937 229 3433.
E-mail address: joykumar.th@notes.udayton.edu (J.S. Thokchom).

0378-7753/$ – see front matter © 2009 Elsevier B.V. All rights reserved.
doi:10.1016/j.jpowsour.2009.11.037

$AlPO_4$ surface in the grain boundary region led to the formation of space charge. The space charge then mediates the transport of conducting ions. Adsorption and desorption processes have been experimentally investigated in the LATP glass–ceramics that allowed a quantitative measurement of the space charge-mediated ionic conduction and the blocking effect [11]. The concentration of the dielectric phases (Li_2O, $AlPO_4$) in turn is dependent on the crystallization temperature and time of the specimen.

In this paper we report the effects of crystallization time and temperature on the ionic conductivity of the LAGP glass–ceramic. The effects include space charge as well as blocking contributions. The role of $AlPO_4$, especially for specimens crystallized at higher temperature and time leading to a dominance of the blocking effect is discussed. The thermally unstable characteristic of the LAGP material is also revealed and discussed in terms of impedance spectroscopy data in this study. The grain and grain boundary contributions especially at low (∼−40 °C) are delineated and the corresponding equivalent circuits are modeled. The highest ambient temperature conductivity, 4.22×10^{-3} S cm^{-1} was achieved for the specimen crystallized at 825 °C for 8 h. The conductivity is of interest from the application point of view.

2. Experimental procedure

2.1. Glass melting

A glass batch [19.75 Li_2O·6.17 Al_2O_3·37.04 GeO_2·37.04 P_2O_5 (mol%)] comprised of reagent grade chemicals such as Li_2CO_3 (Alfa Aesar), Al_2O_3 (Aldrich, particle size <10 μm), GeO_2 (Acros Organics), and $NH_4H_2PO_4$ (Acros Organics) was prepared. The aforementioned chemicals were weighed, mixed, and ground for 10 min in an agate mortar and pestle. For further homogenization, the batch was milled in a glass jar for 1 h using a roller mill. The milled batch was melted in a platinum crucible. Initially, the furnace was heated slowly to 380 °C and held at that temperature for 1 h to release volatile batch components. Subsequently, the furnace was heated with a higher heating rate to 1350 °C and the glass was melted to a homogeneous liquid in about 2 h. After melting, the glass was poured onto a preheated (250 °C) stainless steel (SS) plate and pressed by another preheated (250 °C) SS plate. The processed glass appeared transparent. Subsequently, the cast and pressed glass sheets were annealed at 500 °C for 2 h to release the thermal stresses and then allowed to cool to room temperature. The annealed glass specimens were subsequently crystallized at 775, 800, 825, and 850 °C for 8 h each. Two additional specimens were crystallized at 825 °C for 16 and 24 h. The heating and cooling rates for the crystallization were 3 °C min^{-1}. The crystallization transformed the glass to glass–ceramic that led to a change in the appearance of the glass from colorless transparent to grayish opaque.

2.2. Scanning electron microscopy

Specimens crystallized at 775–850 °C for 8 h and 825 °C for 24 h were fractured, thermally etched, and characterized using a high resolution scanning electron microscope (Hitachi S-4800 HRSEM; Hitachi High Technologies America, Inc., Pleasanton, CA). The thermal etching of the polished specimens was carried out at 650 °C for 3 h.

2.3. AC impedance measurement

An approximately 0.5 μm thick gold coating was sputtered on both sides of the glass–ceramic specimens crystallized at 775–850 °C for 8 h and 825 °C for 24 h. Each gold-coated solid electrolyte was gently assembled into a cell using stainless steel (SS) blocking electrodes in a cell fixture. The fixture containing the SS/electrolyte/SS cell was subsequently placed in a stable fixture holder with attached electrical wires leading to the impedance spectrometer. The impedance measurement on the cell was carried out using a Solartron instrument (Model 1260 with 1287 electrochemical interface) in the 0.1–10^6 Hz frequency range, and Zplot software was used for data acquisition and processing. The AC impedance of the electrolyte was measured in the −40 to 127 °C temperature range at 10 °C intervals. At each temperature, the specimen was equilibrated for 1 h before the impedance measurement. The impedance spectra normally showed two semicircles in the temperature range of −40 to −10 °C, one semicircle in the 3–37 °C range, and a spike at an angle beyond 37 °C. The diameter of each semicircle was fitted using Zview software to obtain the grain and grain boundary resistances. For impedance spectra showing a spike at temperatures beyond 37 °C, a scheme devised earlier [14] was adopted. In addition, the resistances were normalized with respect to the thickness and cross-sectional area of each specimen to compute the grain, grain boundary, and total conductivity.

3. Results and discussion

3.1. Crystal chemistry

During the thermal treatment process, the glass was converted to glass–ceramic, comprising the crystalline phases. All the major reflections reported for the $LiGe_2(PO_4)_3$ lattice matched the XRD pattern of the $Li_{1+x}Al_xGe_{2-x}(PO_4)_3$ ($x = 0.5$) phase [10,13]. In spite of the extensive substitution of Al at the Ge site, the diffraction patterns match closely, which was attributed to the similar ionic radii of Ge^{4+} and Al^{3+}.

Earlier work [13] showed that the $Li_{1+x}Al_xGe_{2-x}(PO_4)_3$ ($x = 0.5$) phase is sensitive to the thermal treatment parameters (temperature and time) and tends to decompose according to Eqs. (1) or (2):

$$Li_{1+x}Al_xGe_{2-x}(PO_4)_3 \rightarrow Li_{1+x}Al_{x-y}Ge_{2-x}(PO_4)_{3-y} + yAlPO_4 \quad (1)$$

$$Li_{1+x}Al_xGe_{2-x}(PO_4)_3 \rightarrow Li_{1+x-0.5y}Al_xGe_{2-x}(PO_{4-y})_3 + yLi_2O \quad (2)$$

The Li_2O and $AlPO_4$ impurities are electrically insulating (dielectric) phases and are expected to influence the electrical conductivity of the glass–ceramic material, even in smaller concentrations.

3.2. Scanning electron microscopy

The Scanning electron microscopy (SEM) micrographs of fractured and thermally etched surfaces of the glass–ceramic specimens crystallized at 775 and 850 °C for 8 h each are shown in Fig. 1(a) and (b). The micrograph for the specimen crystallized at 775 °C for 8 h. Fig. 1(a) shows initial stages of crystallization, whereas the micrograph of Fig. 1(b) shows grown and well-defined crystals. The grains of the specimen crystallized at 775 °C for 8 h are very small in size (≈10 nm) and irregular in shape. As the crystallization temperature increased to 850 °C, the grains and grain boundaries become distinct. The existence of mostly cube-shaped grains having a surface area in the 0.04–0.18 μm^2 range is evident. The grain size distribution remains fairly uniform, though the presence of some irregular and larger (∼1 μm size) grains in the micrograph is also noted (Fig. 1(b)). An increase in grain size with an increase in the crystallization temperature from 775 to 850 °C is apparent. A wide distribution of grain shape and size is observed in the specimen crystallized at 825 °C for 8 h (Fig. 1(c)). The presence of some rod-shape crystallites is also noted in this specimen. The glass–ceramic specimen crystallized at 825 °C for 24 h revealed

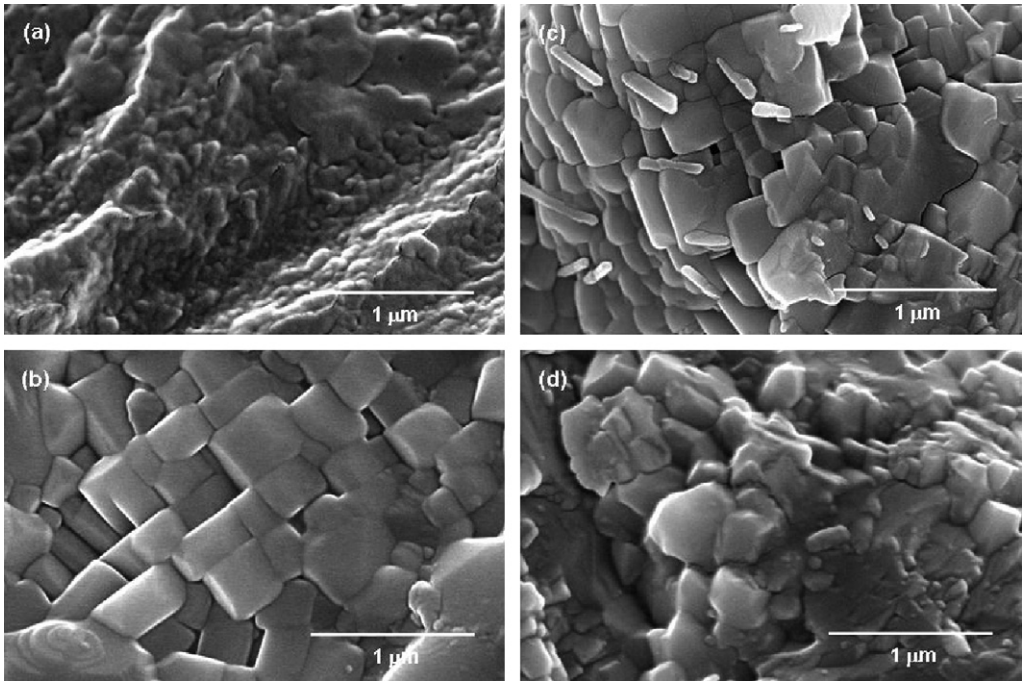

Fig. 1. SEM micrographs of specimens crystallized at (a) 775 °C (8 h), (b) 850 °C (8 h), (c) 825 °C (8 h), and (d) 825 °C (24 h).

the presence of diffuse morphology with a combined inter- and trans-granular fracture pattern (Fig. 1(d)).

3.3. AC impedance data and interpretation

Fig. 2 shows the AC impedance spectra obtained at different temperatures (−40, 3, 47 and 127 °C) for the glass–ceramic specimen crystallized at 825 °C for 8 h. The spectra at −40 °C show a pattern with significant curvature intersecting the Z′ axis towards the high frequency side, which is interpreted as circuit resistance, R_s, external to the specimen. Starting from the intersection and going toward the lower frequency side, segments of depressed semicircles are observed. The semicircle segments are followed by a Warburg-type impedance at low frequencies. The experimental spectra were fitted using the equivalent circuit as shown in the inset of Fig. 2(a) and (b). The semicircle segments were resolved into complete semicircles by using the equivalent circuit and are shown in Fig. 2(a) by broken curves. The first semicircle of the impedance spectra at −40 °C represents the resistance and capacitance of the $[Li_{1.5}Al_{0.5}Ge_{1.5}(PO_4)_3]$ grain, R_g. The semicircle in the mid-frequency region is attributed to grain boundary resistance, R_{gb}. The linear Warburg element at lower frequency is associated with diffusion process. The impedance spectra at −40 °C, Fig. 2(a), reveal comparable grain and grain boundary resistances; however, the grain boundary shows smaller capacitance. The existence of two semicircles in the impedance spectra is observed for all the specimens crystallized at 775, 800, 825, and 850 °C for 8 h in the $-40 \le T \le -10$ °C temperature range. For the temperature range $3 \le T \le 37$ °C only one semicircle representing the total resistance, R_t of the specimen is normally observed (see Fig. 2(b)). The total resistance of the specimen, R_t is thus the sum of R_g and R_{gb}. The fitted equivalent circuit model for the spectra at 3 °C is also shown in the inset of Fig. 2(b). In the temperature range $47 \le T \le 127$ °C, a spike with a slight curvature intersects the Z′ axis in the impedance spectra, Fig. 2(c) and (d). This Z′ offset represents the combined contribution of R_s and R_t. A previously reported scheme for determining the resistance (R_t) of the electrolyte from the impedance spectra showing only a spike was adopted in this study [14]. The resistances R_g, R_{gb}, and R_t were normalized with respect to the thickness and cross-sectional area of each specimen to obtain the grain (σ_g), grain boundary (σ_{gb}), and total conductivity (σ_t) of the specimens.

Fig. 3 displays the AC impedance spectra obtained at different temperatures (−40, 3, 47, and 127 °C) for the glass–ceramic specimen crystallized at 825 °C for 24 h. The major difference as compared to Fig. 2 is that the grain boundary resistance at −40 °C dominates the total resistance indicating, a more resistive grain boundary region perhaps caused by an increased number of $AlPO_4$ nuclei or even well grown crystals. In addition, the temperature range for the existence of the semicircle representing total resistance ($R_t = R_g + R_{gb}$) is extended ($3 \le T \le 67$ °C). Also, a significant increase in the total resistance of the specimen in the temperature range (−40 to 127 °C) is observed for the specimen crystallized at 825 °C for 24 h (Fig. 3) compared to the one crystallized at 825 °C for 8 h (Fig. 2).

3.4. Conductivity

Fig. 4 shows the grain (σ_g), grain boundary (σ_{gb}), and total conductivity (σ_t) plots at −20 °C for the LAGP glass–ceramic specimens crystallized at different temperatures (775, 800, 825, and 850 °C) for a constant time of 8 h. The conductivity data were calculated using Eq. (3):

$$\sigma = \frac{t}{A} \times \left(\frac{1}{R}\right) \tag{3}$$

where t, A, and R are the thickness, area, and resistance of the specimen, respectively. As the crystallization temperature increased from 775 to 850 °C, the grain conductivity, σ_g peaks (9.59×10^{-5} S cm^{-1}) at 825 °C and decreases as the crystallization temperature increases to 850 °C. Similar behavior is exhibited for the grain boundary, σ_{gb}, and total conductivity, σ_t. However, as observed from the plots, the variation in the σ_g is more prominent than the changes in either the σ_{gb} or σ_t. The highest grain conductivity for the specimen crystallized at 825 °C for 8 h is attributed to the optimum time and temperature for the crystallization of the conducting $Li_{1+x}Al_xGe_{2-x}(PO_4)_3$ ($x = 0.5$) phase.

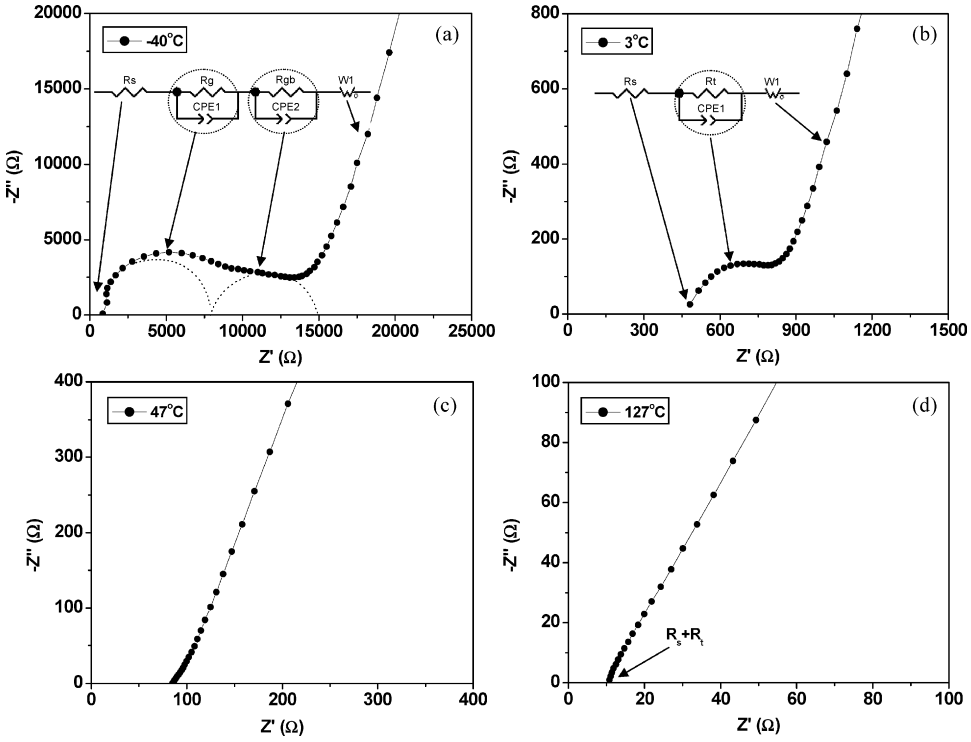

Fig. 2. Impedance spectra at (a) −40 °C, (b) 3 °C, (c) 47 °C, and (d) 127 °C temperatures for the LAGP glass–ceramic specimens crystallized at 825 °C for 8 h. The equivalent circuits are also shown in the insets to the figure.

The AC impedance data as presented in Figs. 2 and 3 clearly demonstrate that the impedance spectroscopy technique provides detailed information regarding the conduction and interaction of lithium ion in the LAGP matrix and impurities. The presence of a $AlPO_4$ phase along the grain boundaries leads to a decrease in the conductivity of the specimen. The total conductivity reflects the characteristics of the grain boundary conductivity since it is the weakest link (see Fig. 4).

Fig. 5 shows the Arrhenius plots of total conductivity, σ_t, in the −40 to 127 °C temperature range for the specimens crystallized at different temperatures (775, 800, 825, and 850 °C) for 8 h. The Arrhenius plots of the specimens are non-linear and

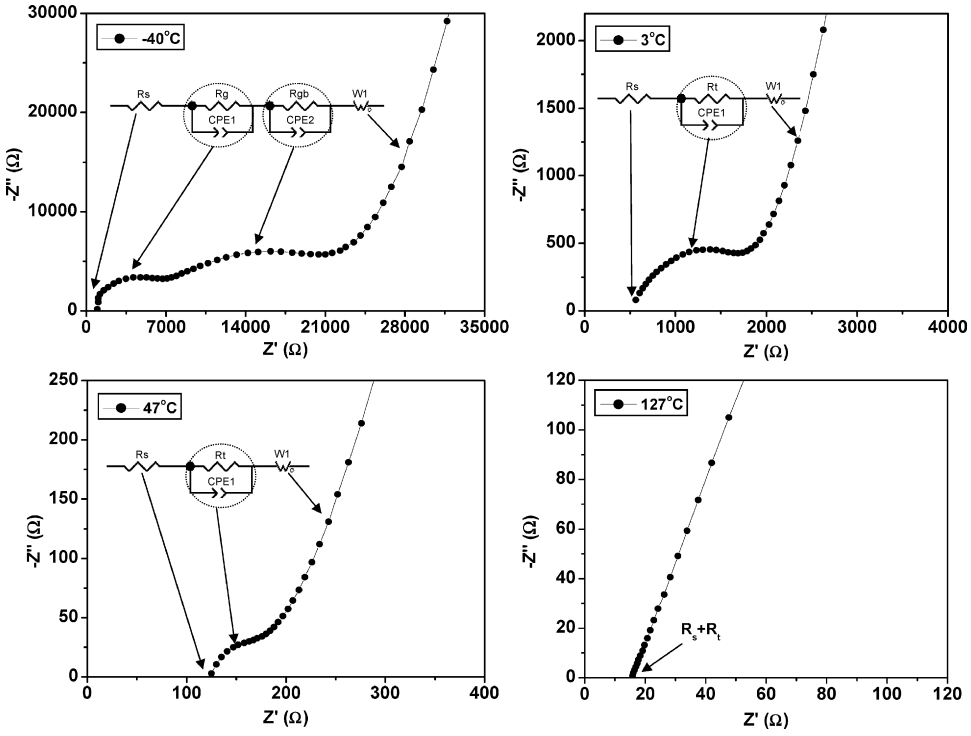

Fig. 3. Impedance spectra measured at different temperatures for the LAGP glass–ceramic specimens crystallized at 825 °C for 24 h. The equivalent circuit models are also shown in the insets to the figure.

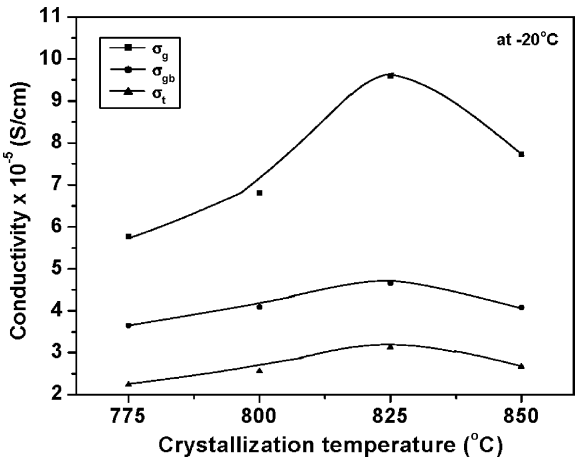

Fig. 4. The grain, grain boundary, and total conductivity plots at −20 °C for the specimens crystallized at 775, 800, 825, and 850 °C for 8 h each.

show two linear segments intersecting at about 37 °C. The non-linearity is attributed to the presence of impurity, the dielectric phase ($AlPO_4$) at the grain boundary, due to the decomposition of the $Li_{1+x}Al_xGe_{2-x}(PO_4)_3$ ($x = 0.5$) crystallite as expressed by Eq. (1). Evidence of such decomposition has been provided in earlier investigations [10,13]. The conductivity data (σ_t), specifically the linear regions of all four specimens, fit the Arrhenius equation as expressed by Eq. (4):

$$\sigma = A \exp\left(\frac{-E_a}{kT}\right) \quad (4)$$

where A is the pre-exponential factor, E_a is the activation energy, and k is the Boltzmann constant. The highest total conductivity, σ_t (4.22×10^{-3} S cm^{-1}) of the LAGP glass–ceramic material at about ambient temperature was obtained by crystallizing the glass at 825 °C for 8 h. The σ_t of the specimen ranges from 6.24×10^{-6} to 8.81×10^{-1} S cm^{-1} in the −40 to 127 °C temperature range. The Arrhenius plots of the specimens clearly demonstrate the role of crystallization temperature and time on conductivity. As the crystallization temperature increases to 850 °C, there is a drop in the conductivity. The reduction in conductivity is very clearly shown in the high temperature region (>37 °C), which is depicted

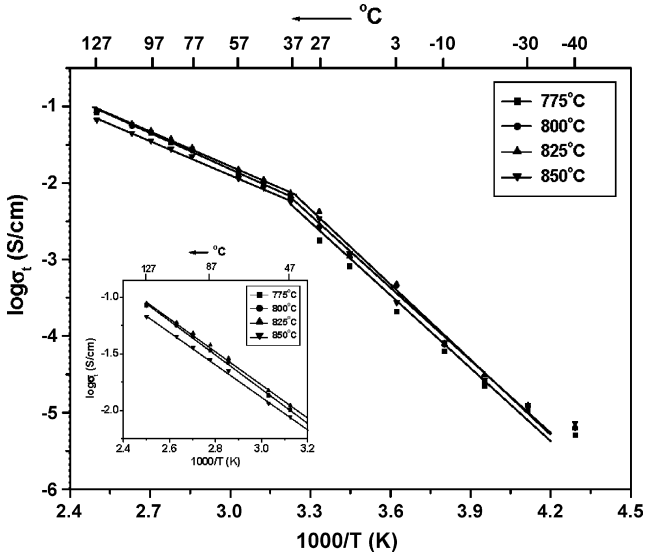

Fig. 5. Arrhenius plots of total conductivity, σ_t, of glass–ceramic specimens crystallized at 775, 800, 825, and 850 °C for 8 h each. Insets show the expanded region of the plot in 47–127 °C temperature range.

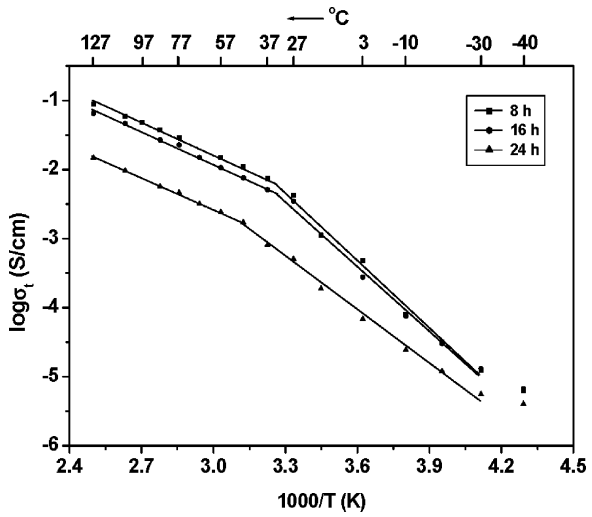

Fig. 6. Arrhenius plots of total conductivity, σ_t, of glass–ceramic specimens crystallized at 825 °C for 8, 16, and 24 h.

by the expanded scale (see inset of Fig. 5). The reduction is attributed to the decomposition of the primary crystalline phase, $Li_{1+x}Al_xGe_{2-x}(PO_4)_3$ and the formation of $AlPO_4$ at the grain boundaries of the specimen as the heat treatment temperature increases from 775 to 850 °C.

Fig. 6 presents the Arrhenius plots of the total conductivity, σ_t, in the −40 to 127 °C temperature range for the specimens crystallized at a constant temperature (825 °C) for 8, 16, and 24 h. The specimen crystallized at 8 h provided the highest conductivity over the entire temperature range. All of the specimens exhibited a non-linearity in the Arrhenius plots with an inflection point at about 37–47 °C. A slight shift in the inflection point from 37 to 47 °C is noted as the crystallization time was increased from 8 to 24 h. A major observation of this study is that as the crystallization time increases, the σ_t decreases, which is again attributed to an increase in the concentration and size of the $AlPO_4$ phase at the grain boundaries, leading to the formation of a highly resistive grain boundary region as evidenced in the impedance spectra (Figs. 2 and 3). The large decrease in total conductivity (in the entire temperature range) of the specimen crystallized at 825 °C for 24 h may be attributed to the diffused microstructure as evidenced in Fig. 1(d).

The activation energies calculated from the Arrhenius plots below and above the inflection temperature (37 °C) for the specimens crystallized at 775, 800, 825, and 850 °C for 8 h, Fig. 5, are 9.93×10^{-20} and 4.81×10^{-20} J, respectively. Table 1 shows the activation energies obtained for the specimens crystallized at 825 °C for 8, 16, and 24 h. The data reveal no change in E_{a1} (the activation energy below the inflection point) when the crystallization time is increased from 8 to 16 h. However, a decrease in E_{a1} is observed when the crystallization time is further increased to 24 h. This decrease in E_{a1} could be due either to the shift in the inflection point in the Arrhenius plot from 37 to 47 + C or to the formation of a well-developed crystal structure. At the higher temperature region (above the inflection point), no significant change in the E_{a2}

Table 1
Activation energies for LAGP glass–ceramic sheets crystallized at 825 °C for different times.

Crystallization time (h)	Lower temperature activation energy, E_{a1} (eV) (−30 to 37 °C)	Higher temperature activation energy, E_{a2} (eV) (37–127 °C)
8	0.61	0.30
16	0.61	0.31
24	0.51	0.30

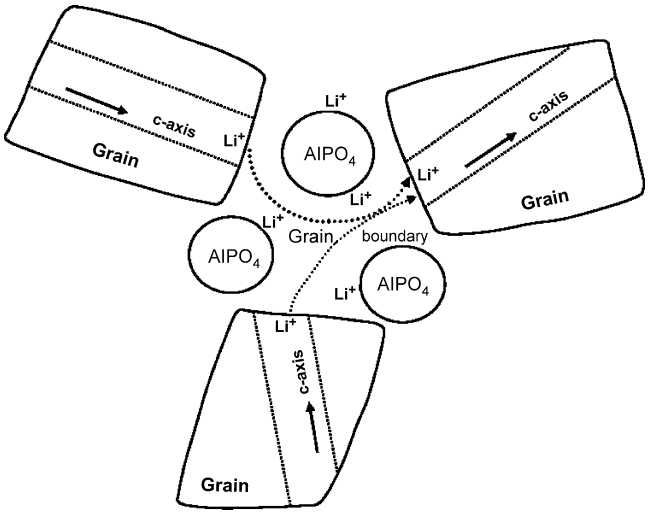

Fig. 7. Schematic representation of lithium ion transport through the network tunnel of LAGP and mediated by space charge.

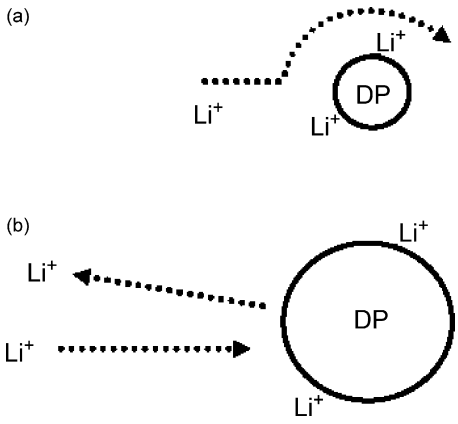

Fig. 8. Schematic representation of space charge and blocking effects and their dependence on the concentration (size) of the dielectric phase (DP).

is observed when the crystallization time at a constant temperature is increased from 8 to 24 h.

The Arrhenius plots of the total conductivity, σ_t of the LAGP glass–ceramic specimens displayed in Figs. 5 and 6 demonstrate the sensitivity of LAGP conductivity on thermal treatment. A decrease in conductivity as the crystallization temperature increased from 825 to 850 °C at a constant time (8 h) and also due to an increase in time from 8 to 24 h at a constant temperature (825 °C) is observed. These characteristics are attributed to the extent of the precipitation of the dielectric phase $AlPO_4$ at the grain boundaries as both the crystallization temperature and time increase.

3.5. Physical models relating to the impurity phase

LAGP glass–ceramic material is a heterogeneous solid with a monoionic (Li^+) conduction. The grain and grain boundary region is schematically shown in Fig. 7. The conduction of lithium ion within the grain takes place through a channel oriented along the *c*-axis.

The space charge region is normally formed due to an accumulation or depletion of local, uncompensated charges in bulk, heterogeneous LAGP glass–ceramic, which possesses an abundance of crystallites (grains) and grain boundaries. The adsorption and desorption of the electroactive species (Li^+) onto a dielectric ($AlPO_4$) surface in the grain boundary region as expressed in Eq. (5) leads to the space charge effect. Space charge then mediates the

$$AlPO_4 + Li^+ \leftrightarrow AlPO_4{:}\ Li^+ \quad (5)$$

transport of conducting ions. This mechanism of ionic transport continues across the bulk of the LAGP glass–ceramic specimen. The inflection point in the Arrhenius plots depends upon the stability of the $AlPO_4$:Li^+ complex. Above 37 °C, the existence of the $AlPO_4$:Li^+ complex and resulting space charge is destroyed because of the thermal energy. The $AlPO_4$:Li^+ complex may be dissociated due to the increased thermal energy ($kT > 4.326 \times 10^{-21}$ J) and Li^+ diffused away from the grain boundaries at temperatures >37 °C.

The concentration and size of $AlPO_4$ influence the conduction of lithium ions in the LAGP solid. The complex, $AlPO_4$:Li^+, becomes a source of an internal field that affects the path of lithium ion conduction. For example, as shown in Fig. 7, after a lithium ion exits from a crystallite it moves through a tortuous path mediated by the $AlPO_4$:Li^+ complex (space charge) and around the $AlPO_4$ crystallite at the grain boundary before it enters another crystallite. The tortuous path is reflected by an increased activation energy before the inflection point in the Arrhenius plots. Above the inflection point there is no $AlPO_4$:Li^+ complex (therefore no space charge) and the activation energy reflects the transport through the *c*-axis of the crystallites and the grain boundaries.

Two physical situations need to be considered when describing the conduction process in a heterogeneous solid such as LAGP. The physical situations are depicted in Fig. 8. When the $AlPO_4$ particles are fewer in number and smaller in size, a dominance of the space charge-mediated conduction is anticipated, Fig. 8(a). The manifestation of this type of conduction is high activation energy. This kind of behavior is anticipated from the LAGP specimen crystallized at a lower temperature and also for a shorter time. With an increase in crystallization time and temperature, the $AlPO_4$ particle may become more abundant and/or larger in size. Such a situation will lead to a blocking effect as depicted in Fig. 8(b). The blocking effect is primarily reflected by lower conductivity resulting from the scattering of ions and subsequent reduction in mobility.

4. Conclusions

A relationship between ionic conductivity and crystallization parameters (temperature and time) was investigated, analyzed, and reported. A glass–ceramic formulation, $Li_{1+x}Al_xGe_{2-x}(PO_4)_3$ ($x = 0.5$) was melted, crystallized at various temperatures and times, characterized using SEM and impedance spectroscopy to delineate the relationship. The Arrhenius plots of the LAGP specimens crystallized at 775, 800, 825, and 850 °C exhibited a non-linear behavior with an inflection point around 37 °C. The inflection point was attributed to the presence of $AlPO_4$ and subsequent formation of a $AlPO_4$:Li^+ complex. The highest conductivity at 27 °C was determined to be 4.22×10^{-3} S cm^{-1} for the glass–ceramic specimen crystallized at 825 °C for 8 h. The concentration of the impurity phase $AlPO_4$ depended upon the crystallization parameters which in turn affected the conductivity. The impurity phase could be a source for the space charge mediation or could block the conduction of ions.

Acknowledgement

The authors acknowledge financial support provided by the University of Dayton Research Institute for preparation of this manuscript.

References

[1] D. Linden, T.B. Reddy, Handbook of Batteries, 3rd ed., McGraw-Hill, New York, 2002.
[2] H. Aono, E. Sugimoto, Y. Sadaoka, N. Imanaka, G. Adachi, J. Electrochem. Soc. 136 (1989) 590.

[3] H. Aono, E. Sugimoto, Y. Sadaoka, N. Imanaka, G. Adachi, J. Electrochem. Soc. 137 (1990) 1023.
[4] G. Adachi, N. Imanaka, H. Aono, Adv. Mater. 8 (1996) 127.
[5] J. Fu, Solid State Ionic 96 (1997) 195.
[6] J. Fu, Solid State Ionics 104 (1997) 191.
[7] B.V.R. Chowdari, G.V. Subba Rao, G.Y.H. Lee, Solid State Ionics 136–137 (2000) 1067.
[8] J.S. Thokchom, B. Kumar, Solid State Ionics 177 (2006) 727.
[9] J.S. Thokchom, B. Kumar, J. Am. Ceram. Soc. 90 (2007) 462.
[10] J.S. Thokchom, B. Kumar, J. Power Sources 185 (2008) 480.
[11] B. Kumar, S. Nellutla, J.S. Thokchom, C. Chen, J. Power Sources 160 (2006) 1329.
[12] B. Kumar, J.S. Thokchom, J. Am. Ceram. Soc. 90 (2007) 3323.
[13] B. Kumar, D. Thomas, J. Kumar, J. Electrochem. Soc. 156 (2009) A506.
[14] J.S. Thokchom, C. Chen, K.M. Abraham, B. Kumar, Solid State Ionics 176 (2005) 1887.